Radio Cherenkov Limits on Diffuse ZeV Neutrino fluxes

Peter GORHAM[1], Kurt LIEWER[1], Charles NAUDET[1] David SALTZBERG[2] & Dawn WILLIAMS[2]

[1]*Jet Propulsion Laboratory, California Institute of Technology*
4800 Oak Grove Drive, Pasadena, CA, 91109, USA
[2]*UCLA Department of Physics & Astronomy, Los Angeles California, USA*

(Received October 19, 2001)

We report on results from about 45 hours of livetime with the Goldstone Lunar Ultra-high energy neutrino Experiment (GLUE). The experiment searches for $\leq$ 10 ns microwave pulses from the lunar regolith, appearing in coincidence at two large radio telescopes separated by about 22 km and linked by optical fiber. The pulses can arise from subsurface electromagnetic cascades induced by interactions of up-coming $\sim$ 100 EeV neutrinos in the lunar regolith. A new triggering method implemented after the first 12 hours of livetime has significantly reduced the terrestrial interference background, and we now operate at the thermal noise level. No strong candidates are yet seen. We report on limits implied by this non-detection, based on new Monte Carlo estimates of the efficiency. We also report on preliminary analysis of smaller pulses, where some indications of non-statistical excess may be present.

KEYWORDS: high-energy neutrinos, radio techniques, the Moon, ultra-high energy cosmic rays

§1. Introduction

Recent accelerator results[1,2] have confirmed the 1962 prediction of Askaryan[3,4] that electromagnetic cascades in dense media should produce strong coherent pulses of microwave Cherenkov radiation. These confirmations strengthen the motivation to use this effect to search for cascades induced by predicted diffuse backgrounds of high energy neutrinos, which are associated with the presence of $\geq 10^{20}$ eV cosmic rays in many models. At neutrino energies of about 100 EeV (1 EeV = 10^{18} eV), cascades in the upper 10 m of the radio-transparent lunar regolith result in pulses that are detectable by large radio telescopes at earth.[5,6] One prior experiment has been reported, using the Parkes 64 m telescope[7] with about 10 hours of livetime.

At frequencies above 2 GHz, ionospheric delay smearing is unimportant, and the signal should appear as highly linearly-polarized, band-limited electromagnetic impulses.[8–10] However, since there are many anthropogenic sources of impulsive radio emission, the primary problem in detecting such pulses is eliminating sensitivity to such interference.

Since 1999 we have been conducting a series of experiments to establish techniques to measure such pulses, using the JPL/NASA Deep Space Network antennas at Goldstone Tracking Facility near Barstow, California.[11] We employ the 70 m and 34 m telecommunication antennas (designated DSS14 and DSS13 respectively) in a coincidence-type system to solve the problem of terrestrial interference, and this approach has proven very effective. Since mid-2000, the project has moved into a new status as an ongoing experiment, and receives more regularly scheduled observations, subject to the constraints imposed by the spacecraft telecommunications priorities of the Goldstone facility.

Although the total livetime accumulated in such an experiment is a relatively small fraction of what is possible with a dedicated system, the volume of material to which we are sensitive, a significant fraction of the Moon's surface to $\sim$ 10 m depth, is enormous, exceeding 100,000 km^3 at the highest energies. The resulting sensitivity is enough to begin to constrain some models for diffuse neutrino backgrounds at energies near and beyond 10^{20} eV. We report on the status of the experiment, and astrophysical constraints imposed by limits from about 45 hours of livetime. We are also improving our understanding of the emission geometry and detection sensitivity through simulations, and describe initial results in extending our sensitivity to pulses of lower amplitude.

§2. Description of Experiment

The lunar regolith is an aggregate layer of fine particles and small rocks, thought to be the accumulated ejecta of meteor impacts with the lunar surface. It consists mostly of silicates and related minerals, with meteoritic iron and titanium compounds at an average level of several per cent, and traces of meteoritic carbon. It has a typical depth range of 10 to 20 m in the maria and valleys, but may be hundreds of meters deep in portions of the highlands.[12] It has a mean dielectric constant of $\epsilon \simeq 3$ and a density of $\rho \simeq 1.7$ gm cm^{-3}, both increasing slowly with depth. Measured values for the loss tangent vary widely depending on iron and titanium content, but a mean value at high frequencies is $\tan\delta \simeq 0.003$, implying a field attenuation length at 2 GHz of $(\alpha)^{-1} = 9$ m.[13]

2.1 Emission geometry & Signal Characteristics

In Fig. 1 we illustrate the signal emission geometry. At 100 EeV the interaction length L_{int} of an electron or muon neutrino for the dominant deep inelastic hadronic

scattering interactions (averaging over the charged and neutral current processes) is about 60 km[15] ($R_m = 1740$ km). Upon interaction, a $\sim$ 10 m long cascade then forms as the secondary particles multiply, and compton scattering, positron annihilation, and other scattering processes then lead to a $\sim$ 20% negative charge excess which radiates a cone of coherent Cherenkov emission at an angle of 56°, with a FWHM of 1°. The radiation propagates in the form of a sub-ns pulse through the regolith to the surface where it is refracted upon transmission.

Because the angle for total internal reflection (TIR) of the radiation emitted from the cascade is to first order the complement of the Cherenkov angle, we consider for the moment only neutrinos that cascade upon emerging from a penetrating chord through the lunar limb. Under these conditions the typical neutrino cascade has an upcoming angle with respect to the local surface of

$$\theta_{up} \;=\; \sin^{-1}\left(\frac{L_{int}}{2R_m}\right) \qquad (2.1)$$

which implies a mean of $\theta_{up} \sim 1^\circ$ at 10^{20} eV.

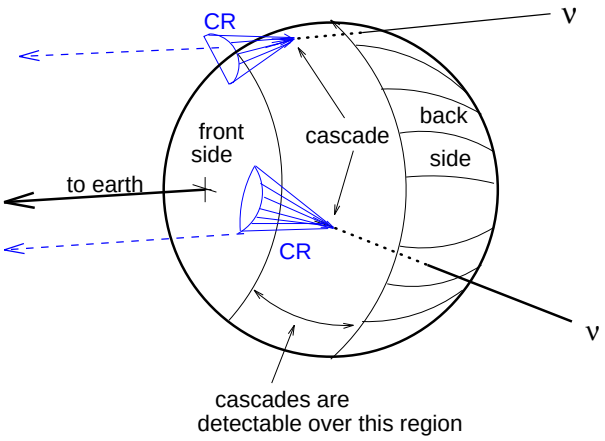

Fig. 1. Schematic of the geometry for lunar neutrino cascade event detection.

At the regolith surface the resulting microwave Cherenkov radiation is refracted strongly into the forward direction. Scattering from surface irregularities and demagnification from the interface refraction gradient fills in the Cherenkov cone, and results in a larger effective area of the lunar surface over which events can be detected, as well as a greater acceptance solid angle. These effects are discussed in more detail in section III.A.

2.2 Antennas & receivers

The antennas employed in our search are the shaped-Cassegrainian 70 m antenna DSS14, and the beam waveguide 34 m antenna DSS13, both part of the NASA Goldstone Deep Space Network (DSN) Tracking Station. DSS13 is located about 22 km to the SSE of DSS14. The S-band (2.2 GHZ) right-circular-polarization (RCP) signal from DSS13 is filtered to 150 MHz BW, then downconverted with an intermediate frequency (IF) near 300 MHz. The band is then further subdivided into high and low frequency halves of 75 MHz each, and no overlap. These IF signals are then sent via an analog fiber-optic link to DSS14. At DSS14, the dual polarization S-band signals are downconverted with the same 300 MHz IF, and bandwidths of 100 MHz (RCP) and 40 MHZ (LCP) are used. A third signal is also employed at DSS14: a 1.8 GHz (L-band) feed which is off-pointed by $\sim 0.5^\circ$ is used as a monitor of terrestrial interference signals; the signal is downconverted in the same manner as the other signals and has a 40 MHz bandwidth.

2.3 Trigger system

The experimental approach in our initial 12 hours of observations was to use a single antenna trigger with dual antenna data recording.[11] This was accomplished by using the local S-band signals as DSS14 to form a 2-fold coincidence with an active veto from the L-band interference monitor. Since any system with an active veto is subject to potential unforeseen impact on the trigger efficiency, we have now developed an approach which utilizes signals from both antennas to form a real-time dual-antenna trigger, with no active veto.

Fig. 2 shows the layout of the trigger. The four triggering signals from the two antennas are converted to unipolar pulses using tunnel-diode square-law detectors. Stanford Research Systems SR400 discriminators are used for the initial threshold level, and these are set to maintain a roughly constant singles rate, typically 0.5-1 kHz/chan for DSS14 and 30 kHz/chan for DSS13 (DSS13's rate is higher due to a lower threshold, compensating for the reduced aperture size). A local coincidence is then formed for each antenna's signals. The DSS14 coincidence between both circular polarizations ensures that the signals are highly linearly polarized, and the DSS13 coincidence helps to ensure that the signal is broadband.

Fig. 3 indicates the timing sequence for a trigger to form (negative logic levels are used here). A local coincidence at DSS14, typically with a 25 ns gate, initiates the trigger sequence. After a 65 μs delay, a 150 μs gate is opened (the delays compensate for the 136 μs fiber delay between the two antennas). This large time window encompasses the possible geometric delay range for the moon throughout the year. Use of a smaller window is possible but would require delay tracking and a thus more stringent need for testing and reliability; use of a large window avoids this and a tighter coincidence can then be required offline.

If a 25 ns local coincidence now forms between the two DSS13 signals within the allowed 150 μs window, a trigger is formed. The sampling scopes are then triggered, and a 250 μs record, sampled at 1 Gs/s, is stored. The average trigger rate, due primarily to random coincidences of thermal noise fluctuations, is about 1.6 mHz, or 1 trigger every 5 minutes or so. Terrestrial interference triggers are uncommon (a few percent of the total), but can occasionally increase in number when a large burst of interference occurs at either antenna, with DSS14 more

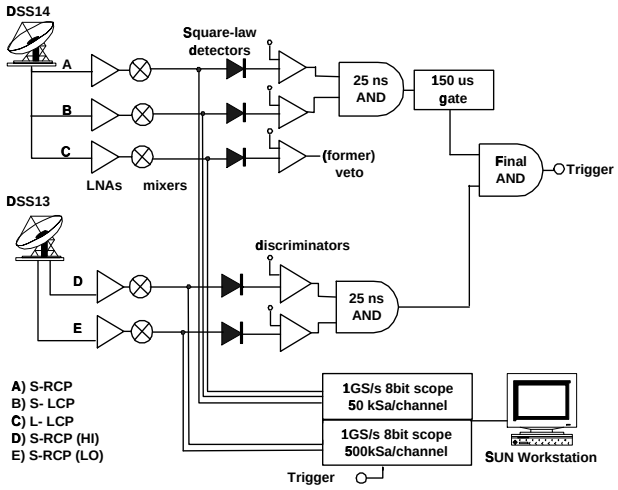

Fig. 2. The GLUE trigger system used for the lunar neutrino search.

sensitive to this effect. The deadtime per event is about 6 s; thus on average we maintain about 99% livetime during a run.

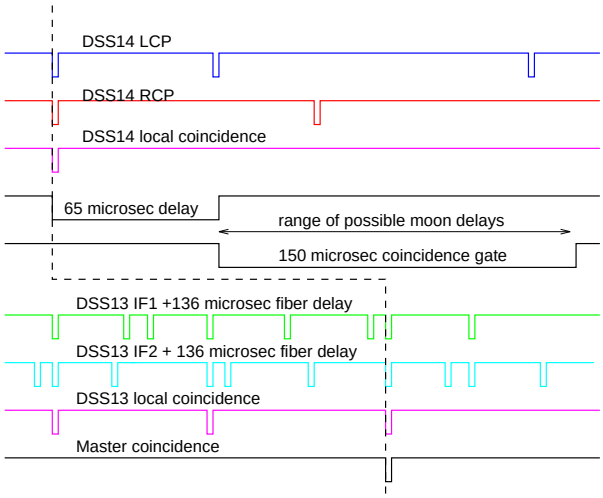

Fig. 3. A timing diagram for the GLUE trigger system.

2.4 Geometric and timing considerations.

As noted above, the precise geometry of the experiment is a crucial discriminator for events from the moon. Let $\vec{S}$ be a unit direction vector to the moon, and $\vec{B}$ be the baseline vector between the two antennas. The projected baseline is $B_\perp = \vec{B} \cdot \vec{S}$, and the relative delay between the two antennas is $\tau = c^{-1}|\vec{B}| \cos\theta$ where θ is the apparent angle of the moon with respect to the baseline vector. For $|\vec{B}| \simeq 22$ km, we have a maximum delay difference of about $\tau_{max} = 73$ μs. Wavefront curvature effects due to the fact that the moon is not at infinite distance lead to corrections of order 1 ns.

A much larger effect arises from the fact that detectable events can occur anywhere on the moon's surface within the antenna primary beam, or even in its sidelobes. This produces a possible spread in the differential delay of the received pulses at the two antennas, which has the maximum value $\Delta\tau = c^{-1}|\vec{B}| \sin\Delta\theta \simeq 630$ ns, given that the angular diameter of the moon is $\Delta\theta = 0.5°$.

The antenna beamwidths for a frequency of 2.2 GHz, between the first Airy nulls, are nominally 0.27° for the 70 m, and 0.56° for the 34 m. In fact, for our present observations, we intentionally defocus the 70 m beam to provide a better match to the 34 m beam (with some loss of efficiency), and this means that we must in fact account for the entire 630 ns window when determining whether a triggered event has a delay that is appropriate for lunar origin.

2.5 Calibration.

Timing and amplitude calibration are accomplished by a series of interlocking methods. Since we are critically dependent on timing to accurately estimate our delays, we internally calibrate the back-end trigger system using a synthesized IF pulse signal, giving precision of order 1 ns. We then use a 2.2 GHz monocycle pulse generator projected at the antennas externally using a microwave horn to calibrate the cross-channel delays of each antenna to a precision of typically 1-2 ns. The cross-polarization timing at DSS 14 is checked with a second method which utilizes the fact that the thermal radiation from the limb of the moon is significantly linearly polarized (from differential Fresnel effects), and this introduces an LCP/RCP correlation that is easily detected.

Cross-antenna timing calibration is accomplished by cross-correlating a 250 μs thermal noise sample of a bright quasar, typically 3C273, recorded from both antennas at the same time and in the same polarization, using the identical data acquisition system used for the pulse detection. This procedure establishes the delay offset between the two antennas, which is of order 138 μs, but can change from run to run by tens to even hundreds of ns because of changes in fiber routing for different experiments.

Amplitude calibration is accomplished by the standard methods of radio astronomy, by referencing to a known thermal noise source at a known temperature. The measured system temperature during a run then fixes the value of the noise level and therefore the overall sensitivity. We also check linearity for pulsed transient response using the monocycle generators and this ensures that we have the dynamic range required to see large pulses.

2.6 Event example.

Figure 4 shows a typical event. The top two panes contain the DSS 14 LCP and RCP signals, and a narrow pulse is present in both polarizations, indicating a

broadband spectral content, and a high degree of linear polarization. The overlain rectangle on each pulse is a fit to the pulse width and is used in the visual analysis. The pulse power is normalized to the local mean power over a 250 μs window (the statistics are checked separately to ensure that they follow the expected exponential distribution). In the third and fourth panes, the two channels from DSS13 are shown. In the fifth pane from the top the L-band offset feed signal from DSS 14 is shown, and no noise is present which would indicate RFI. Finally, the bottom pane shows a sum of the (negative) logic signals that formed the trigger, showing that there was good alignment. The measured delay relative to the expected moon time is shown as -1.1 μs in this case, slightly larger than what can be nominally allowed. Systematic timing offsets from channel to channel are typically less than 10 ns in these data.

In practice our first pass analysis requires a pulse of equivalent 6σ significance. In terms of normalized power, we require a value of at least 20 times the mean power in each polarization to be considered as a candidate. To date we have seen no such candidates in 45 hours of livetime.

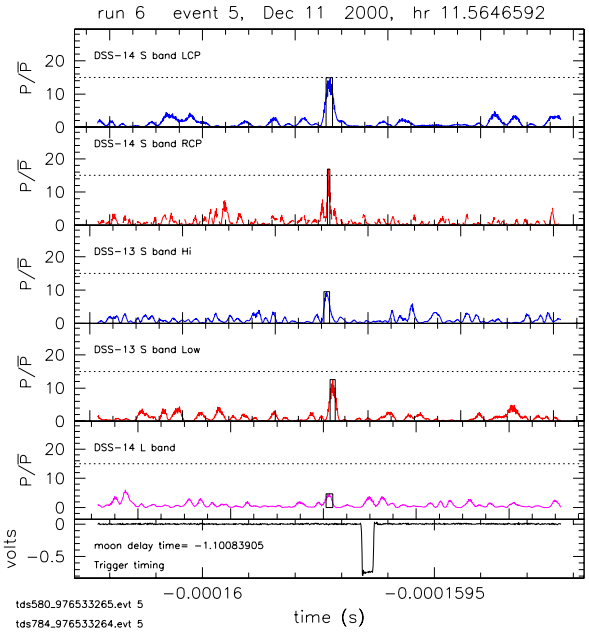

Fig. 4. An example of a triggered event. The displayed signals are, from top to bottom: the left circular polarized intensity at DSS14; the right-circular polarization intensity; the high-band intensity at DSS13; the low-band intensity at DSS13; the L-band off-axis interference monitor (no interference present); and finally the trigger logic summed discriminator pulses (including a 100 ns delay relative to the pulse. The box drawn around each pulse shows a fitted width indicator used for visual inspection of the events.

§3. Estimated sensitivity

Estimates of the sensitivity of radio telescope observations usually involve systems that integrate total power for some time constant Δt which is in general much longer than the antenna's single temporal mode duration which is given by the inverse of the bandwidth: $\tau = (\Delta\nu)^{-1}$. Since the pulses of interest in our experiment are much shorter than this time scale, the observed pulse structure of induced voltage in the antenna receiver is determined only by the bandpass function; that is, the pulses are band-limited. Thus the typical dependence of sensitivity on the factor $\sqrt{\Delta t \Delta\nu}$ does not obtain; this factor is always unity in band-limited pulse detection.

Because much of the theoretical work in describing such pulses has been done in terms of field strength rather than power, we analyze our sensitivity in these terms as well. Such analysis is also compatible with the receiving system, which records antenna voltages proportional to the incident electric field, and leads to a more linear analysis. It also yields signal-to-noise ratio estimates which are consistent with Gaussian statistics, since thermal noise voltages are described by a Gaussian random process.

The expected field strength per unit bandwidth from a cascade of total energy W_T can be expressed as:[8–10]

$$E_0\ (\mathrm{V\ m^{-1}\ MHz^{-1}}\ ) = \frac{2.53\times10^{-7}}{R}\left(\frac{W_T}{1\ \mathrm{TeV}}\right) \times \frac{\nu}{\nu_0}\left(\frac{1}{1+0.4(\nu/\nu_0)^{1.44}}\right), \quad (3.1)$$

where R is the distance to the source in m, ν is the radio frequency, and the decoherence frequency is $\nu_0 \simeq 2500$ MHz for regolith material (ν_0 scales mainly by radiation length). For typical parameters in our experiment, a 10^{19} eV cascade will result in a peak field strength at earth of $E \simeq 0.5$ μV m^{-1} for a 70 MHz BW. Equation 3.1 has now been verified to within factors of 2 through accelerator tests[1,2] using silica sand targets and γ-ray-bunch-induced cascades with $W_T \leq 10^{19}$ eV per bunch.

Given that the use of a dual antenna trigger has virtually eliminated the problem of terrestrial interference that was the primary limitation to the sensitivity of the one previous experiment,[7] we can now express the minimum detectable field strength E_{min} for each antenna in terms of the induced signal and the thermal noise background.

The expected signal strength E_0 induces a voltage at the antenna receiver given by

$$v_s = h_e E_0 \Delta\nu \quad (3.2)$$

where the antenna effective height h_e is given by[14]

$$h_e = 2\sqrt{\frac{Z_a \eta A}{Z_0}}\cos\theta_p \quad (3.3)$$

where Z_a is the antenna radiation resistance, η and A are the antenna efficiency and area, respectively, $Z_0 = 377\ \Omega$ is the impedance of free space, and θ_p the polarization angle of the antenna with respect to the plane of polarization of the radiation.

The average thermal noise voltage in the system is given by

$$v_n \;=\; \sqrt{4kT_{sys}Z_T\Delta\nu}\;. \qquad (3.4)$$

Here k is Boltzmann's constant, T_{sys} is the system thermal noise temperature, and Z_T the termination impedance of the receiver. If we assume that $Z_a \approx Z_T$ then the resulting SNR S is

$$S \;\equiv\; \frac{v_s}{v_n} \;=\; E_0\cos\theta_p\sqrt{\frac{\eta A\Delta\nu}{kT_{sys}Z_0}}\;. \qquad (3.5)$$

The minimum detectable field strength ($E_0 \rightarrow E_{min}$) is then given by

$$E_{min} \;=\; S\sqrt{\frac{kT_{sys}Z_0}{\eta A\Delta\nu}}\;\frac{1}{\cos\theta_p}\;. \qquad (3.6)$$

Combining this with equation 3.1 above, the threshold energy for pulse detection is

$$W_{thr}(\mathrm{EeV}) \;\simeq\; 4.0\left(\frac{E_{min}}{1\mathrm{V\ m^{-1}MHz^{-1}}}\right)\left(\frac{R}{1\ \mathrm{m}}\right)\frac{\nu_0}{\nu} \times\left[1+0.4\left(\frac{\nu}{\nu_0}\right)^{1.44}\right]\;. \qquad (3.7)$$

For the lunar observations on the limb, which make up about 85% of the data reported here, $T_{sys} \simeq 110$ K, $\nu = 2.2$ GHz, and the average $\Delta\nu \simeq 70$ MHz. For the 70 m antenna, with efficiency $\eta \simeq 0.8$, the minimum detectable field strength is $E_{min} \simeq 1.2\times10^{-8}$ V m^{-1} MHz^{-1} for $\cos\theta_p = 0.7$. The estimated threshold energy for these parameters is $W_{thr} = 2.8\times10^{19}$ eV, assuming a detection level of $S = 5$ (5σ) per IF at DSS14 (with a somewhat lower requirement at DSS13 in coincidence).

3.1 Monte Carlo results

To estimate the effective volume and acceptance solid angle as a function of incoming neutrino energy, events were generated at discrete neutrino energies, including the current best estimates of both charged and neutral current cross sections,[15] and the Bjorken-y distribution. Both electron and muon neutrino interactions were included, and Landau-Pomeranchuk-Migdal effects in the shower formation were estimated.[10] At each neutrino energy, a distribution of cascade angles and depths with respect to the local surface was obtained, and a refraction propagation of the predicted Cherenkov angular distribution was made through the regolith surface, including absorption and reflection losses and a first order roughness model. Antenna thermal noise fluctuations were included in the detection process.

A portion of the simulation is shown in Fig. 5. Here the flux density is shown as it would appear projected on the sky, with (0,0) corresponding to the tangent to the lunar surface in the direction of the original cascade. The units are Jy (1 Jy $= 10^{-26}$ W m^{-2} Hz^{-1}) as measured at earth, and the plot is an average over several hundred events at different depths and a range of θ_{up} consistent with a 10^{20} eV neutrino interaction, averaging over inelasticity effects and a mixture of electron and muon neutrinos consistent with decays from a hadronic $\pi^{\pm}$ source.

Although the averaging has broadened the distribution somewhat, a typical cascade still produces a flux density pattern of comparable angular size. The angular width of the pattern directly increases the acceptance solid angle, and the angular height increases the annular band of the lunar surface over which neutrino events can be detected, as indicated in Fig. 1. The net effect is that, although the specific flux density of the events are lowered somewhat by refraction and scattering, the effective volume and acceptance solid angle are significantly increased. The neutrino acceptance solid angle, in particular, is about a factor of 50 larger than the apparent solid angle of the moon itself.

3.2 EHE cosmic rays

We have noted above that the refraction geometry of the regolith favors emission from cascades that are upcoming relative to the local regolith surface. Thus to first order EHE cosmic ray events, which cascade within a few tens of cm as they enter the regolith, will not produce detectable pulses since their emission with be totally internally reflected within the regolith. This effect has been now demonstrated in an accelerator experiment.[2]

This conclusion does not account for several effects however. These effects are illustrated in Fig. 6. In Fig. 6A, the varying surface angles due surface roughness on scales greater than a wavelength will lead to escape of some radiation from cosmic ray cascades. Fig. 6B illustrates that, because the Cherenkov angular distribution is not infinitely narrow arround the Cherenkov angle (FWHM $\sim 1^\circ$), emission at angles larger then the Cherenkov angle can escape total internal reflectance. In Fig. 6C cascades from cosmic rays that enter along ridgelines can encounter a change in slope of the local surface that results in more efficient transmission of the radiation.

Even if total internal reflection strongly suppresses detection of cosmic rays in cases A and B, the latter case C of favorable surface geometry along ridgelines or hilltops will lead to some background of EHE cosmic ray events. We have not as yet made estimates of this background.These conclusions also apply of course to the fraction of neutrinos which interact on entering the regolith as well as those which interact near their projected exit point. Thus we have not yet accounted for all of the possible neutrino events as well as the cosmic ray background events.

Fig. 6D shows the formation zone aspect of the process of Cherenkov emission from near-surface cosmic ray cascades. This constraint may suppress Cherenkov production even if surface roughness and the width of the Cherenkov distribution would otherwise favor some escape of emission.

It has now been conclusively shown[16] that coherent Cherenkov emission is a process involving the bulk dielectric properties of the radiating material. Cherenkov radiation is induced over a macroscopic region of the dielectric (with respect to the scale of a wavelength), and

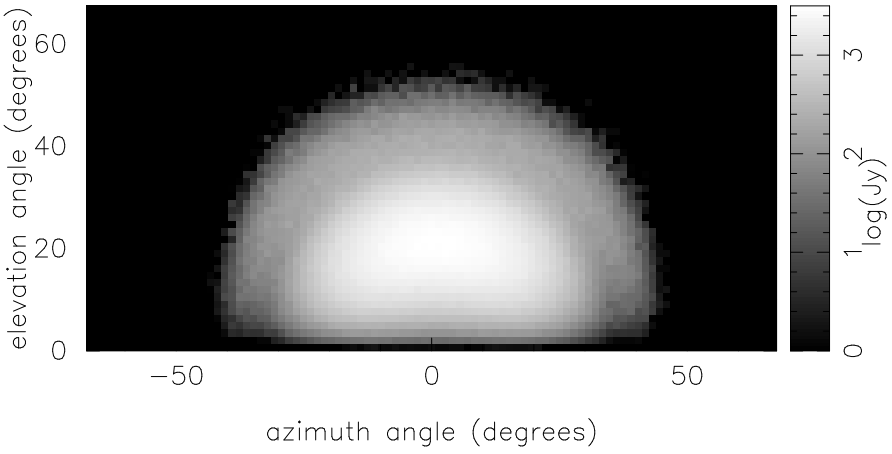

Fig. 5. The microwave Cherenkov radiation pattern from an event in the lunar regolith. This plot shows a map of the average intensity projected onto the sky that would result from a typical 100 EeV neutrino cascade. The pattern differs markedly from the initial Cherenkov distribution due to propagation & surface refraction effects.

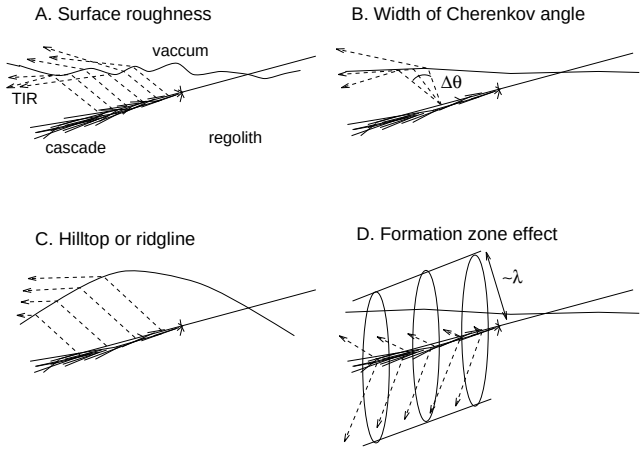

Fig. 6. Various effects associated with EHE cosmic ray hadron interactions.

does not even require that the charged particles enter the dielectric for radiation to be produced—a proximity of several wavelengths or less is sufficient.[17] A corollary to this result is that a cascade travelling along very near a boundary of the dielectric will not radiate (or radiate only weakly) into the hemisphere with the boundary.

Thus in the case of a cosmic ray entering the regolith at near grazing incidence (say within $\sim 1^\circ$) the resulting cascade reaches maximum within ~ 3 cm of the surface, still less than a wavelength for S-band observations. We therefore expect that the suppression of Cherenkov emission in such events significantly reduces our sensitivity to cosmic rays. Such effects have not been included yet in other estimates[9,18] of the cosmic ray detection efficieny of such experiments.

§4. Results

Figure 7 plots the predicted fluxes of EHE neutrinos from a number of models including AGN production[23] gamma-ray bursts,[19] EHE cosmic-ray interactions,[22] topological defects,[21,25] and the Z_0 burst scenario.[24] Also plotted are limits from about 70 days of Fly's Eye livetime[20] (accumulated in several years of runtime), which apply only to electron neutrino events.

Table I. Differential limits on mono-energetic EHE neutrino fluxes.

$\log_{10}$(Neutrino Energy) (eV)	$\log_{10}(EdF/dE)$ (cm^{-2} s^{-1} sr^{-1})
19.0	-13.14
19.5	-14.14
20.0	-14.92
20.5	-15.39
21.0	-15.73
21.5	-15.90
22.0	-16.03
22.5	-16.14
23.0	-16.30

Our initial 90% CL limit, for 30 hours of livetime is shown plotted with diamonds (see also Table 1), based on the observation of no events above an equivalent 6σ level amplitude (referenced to the 70 m antenna) consistent with the direction of the moon. These limits assume

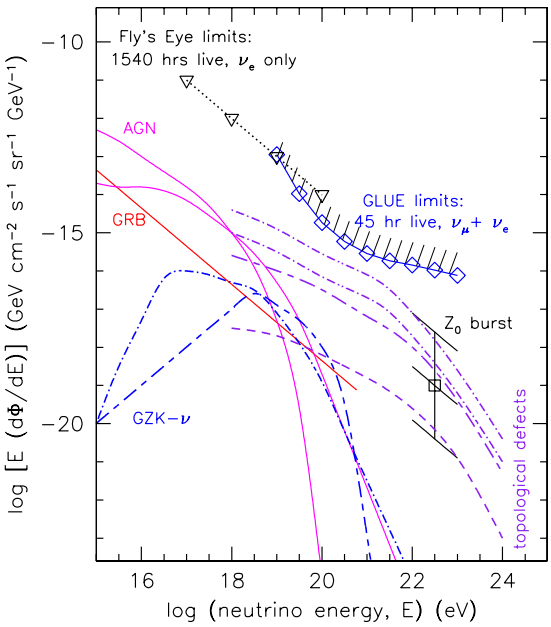

Fig. 7. Plot of model neutrino fluxes and limits from the Fly's Eye experiment and the present work.

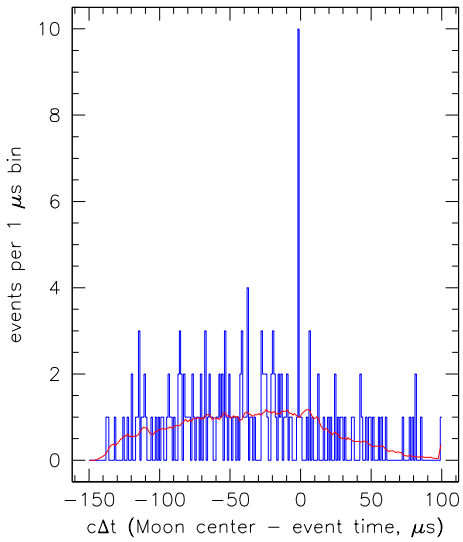

Fig. 8. Low amplitude event histogram of GLUE data in delay with respect to the moon center delay. The overlain histogram is the expected background level. An excess occurs near zero delay, with a 1.3 microsecond offset.

a monoenergetic signal at each energy; thus they are differential limits and independent of source spectral model, and represent the most conservative limits we can apply. Our limits just begin to constrain the highest topological defect model[25] for which we expected a total of order 1–2 events.

In addition to the limits set above from the non-observation of events above, we have also analyzed events which triggered the system, but did not pass our more stringent software amplitude cuts. A sample of events was prepared by applying our standard cuts to remove terrestrial interference events. We required somewhat tighter timing that the hardware trigger, as well as band-limited pulse shape, but allowed smaller amplitudes, typically corresponding to $\sim 4.5\sigma$ at DSS14, and about 3σ at DSS13. The results are shown in Fig. 8, where the passing events have been binned according to their delay timing with respect to the expected delay from an event at the center of the moon. The background level (solid line) has been determined by randomizing the UT of the events and indicates the somewhat non-uniform seasonal coverage of our observations.

An excess is observed in the vicinity of zero delay where the lunar events are expected to cluster. At present there is a $\sim 1.3\mu$s offset from zero delay; this is too large to be accounted for by differential delays to the lunar limb, which can produce offsets of up to ~ 650 ns.

If the offset can be ascribed to experimental systematic error, and the low amplitude events are interpreted as pulses of lunar origin which arise from ultra-high energy cosmic ray events, then the implied aperture for $\geq 10^{20}$ eV cosmic rays is of order 3×10^5 km^2 sr. Such a large cosmic-ray aperture (about 10% of the lunar surface area within our average beam) implies a much higher efficiency for detection of radio emission from cosmic ray events than expected from the arguments described above. Further study of the low amplitude events is in progress.

§5. Conclusions

We have developed a robust system for observing microwave pulses produced in the lunar regolith by electromagnetic particle cascades above $\sim 10^{19}$ eV. We have operated this system to achieve a livetime of 45 hours, with no large apparent signals detected to date. We have set conservative upper limits on the diffuse cosmic neutrino fluxes over the energy range from 10^{19-23} eV. We have also begun to analyze smaller events and have some preliminary indications that a signal may be present, but requiring further study.

We thank Michael Klein, George Resch, and the staff at Goldstone for their enthusiastic support of our efforts. This work was performed in part at the Jet Propulsion Laboratory, California Institute of Technology, under contract with NASA, and supported in part by the Caltech President's Fund, by DOE contract DE-FG03-91ER40662 at UCLA, the Sloan Foundation, and the National Science Foundation.

1) P. W. Gorham, D. P. Saltzberg, P. Schoessow, et al., 2000, Phys. Rev. E. **62**, 8590.
2) D. Saltzberg, P. Gorham, D. Walz, et al. 2001, Phys. Rev. Lett., **86**, 2802.

3) G. A. Askaryan,1962, JETP 14, 441
4) G. A. Askaryan,1965, JETP 21, 658
5) I. M. Zheleznykh, 1988, Proc. Neutrino '88, 528.
6) R. D. Dagkesamanskii, & I. M. Zheleznyk, 1989, JETP 50, 233
7) T. H. Hankins, R. D. Ekers & J. D. O'Sullivan, 1996, MNRAS 283, 1027.
8) E. Zas, F. Halzen,, & T. Stanev, 1992, Phys Rev D 45, 362
9) J. Alvarez–Muñiz, & E. Zas, 1996, Proc. 25th ICRC, ed. M.S. Potgeiter et al.,7,309.
10) J. Alvarez–Muñiz, & E. Zas, 1997, Phys. Lett. B, 411, 218
11) P. Gorham, et al., Proc. 26th ICRC, HE 6.3.15, astro-ph/9906504
12) D. Morrison & T. Own, 1987 *The Planetary System*, (Addison-Wesley: Reading,MA)
13) G. R. Olhoeft & D. W. Strangway, 1975, Earth Plan. Sci. Lett. 24, 394
14) J. D. Kraus, 1988, *Antennas*, (McGraw-Hill:New York)
15) R. Gandhi, 2000, hep-ph/0011176.
16) T. Takahashi, Y. Shibata, K. Ishi, et al. 2000, Phys Rev. E, 62, 8606
17) R. Ulrich, 1966, Zeit. Phys., 194, 180.
18) J. Alvarez–Muñiz, & E. Zas,, 2001, this proceedings.
19) E. Waxman & J. N. Bahcall,, 2000, Ap.J. 541, 707, astro-ph/9902383
20) Baltrusaitas, R.M., Cassiday, G.L., Elbert, J.W., et al 1985, Phys Rev D 31, 2192.
21) Bhattacharjee, P., Hill, C.T., & Schramm, D.N, 1992 PRL 69, 567.
22) Hill, C.T., & Schramm, D.N., 1985, Phys Rev D 31, 564.
23) Mannheim, K., 1996, Astropart. Phys 3, 295.
24) T. Weiler, 1999, hep-ph/9910316.
25) S. Yoshida, H. Dai, C. C. H. Jui, & P. Sommers, 1997, ApJ 479, 547.